Research Paper

Linking particle properties to layer characteristics: Discrete element modelling of cohesive fine powder spreading in additive manufacturing

Yi He [*], Ali Hassanpour, Andrew E. Bayly

School of chemical and process engineering, University of Leeds, Leeds, United Kingdom

ABSTRACT

Particle properties play a key role in determining the flowability of cohesive fine powders and consequently the quality of parts fabricated by additive manufacturing. However, how the characteristics of a spread powder layer are linked to particle properties remains not well understood, largely due to the limitations of available numerical models and characterisation approaches. This study thus established an efficient discrete element modelling framework to address these issues, combining GPU computing with a novel methodology for particle stiffness scaling. The validity of the DEM model was verified on both packing and spreading of cohesive fine powders. The effect of particle cohesion on the characteristics of a spread powder layer was systematically analysed for non-cohesive and weakly to strongly cohesive powders. The structure of spread powder layer was qualitatively illustrated and quantitatively evaluated by not only commonly used metrics, such as coordination number, packing density and surface profiles but also particle clustering and pore characteristics. While reducing particle cohesion leads to an enhanced powder flowability, different regimes were identified in the relationship between layer characteristics and particle cohesion. The results showed that powder spreadability has a complicated dependence on the strength of particle cohesion, where the underlying mechanisms can be understood in part via a dimensionless inertial length. These findings not only provide valuable metrics to quantitatively evaluate the quality of a spread powder layer, but also enable a better understanding of the physics underlying the spreading of cohesive fine powders.

1. Introduction

Additive manufacturing (AM) has attracted significant attentions across a broad range of industrial sectors due to its advantages of fast prototyping and near-net-shape production. In powder-bed-based AM processes, particles within selected areas are fused together by either a high energy source (laser, electron beam or plasma) or a binder, in a layer-upon-layer fashion to build up objects of complex shapes [1]. The quality of additively manufactured part is affected by many parameters, including both process parameters such as laser power, scanning speed, spot size, preheat temperature and feedstock properties such as powder surface chemistry and morphology [2–6]. In these processes, powder material is often deposited with the aid of a spreading blade or a rotating roller, in which particles are subject to localized shearing and compression. The quality of spread powder layer plays a key role in determining residual porosity and sintering strength and hence the structural and mechanical properties of the fabricated parts [7–10]. A poor spreading may lead to undesirable features, such as patchy

coverage, size segregation and non-uniform density distribution. An in-depth understanding of the link between microscopic particle properties and characteristics of a spread powder layer is thus critical for the evaluation of powder spreadability and optimization of part quality.

Considerable efforts have been devoted to investigating powder spreading process using both experimental and numerical approaches. Standardized tests have been used to assess powder flowability for powder bed fusion, such as funnel flowmeter, static angle of repose, rotating drum, shear cell, FT4 powder rheometer and ball indentation [11–15]. However, stress conditions within these tests are different from that of powder spreading. A testing device of relevance to the process conditions is thus required to either probe powder behaviour during spreading or to measure powder spreadability [16–20]. Van den Eynde et al. [17] proposed a lab-scale powder spreader to mimic powder spreading in laser sintering, which allows the overall packing density of deposited powder layer to be measured on a balance. Sun et al. [18] developed a powder deposition system identical to that used in an EBM machine, where surface quality of spread powder layer is analysed by

* Corresponding author.
E-mail addresses: y.he1@leeds.ac.uk (Y. He), A.E.Bayly@leeds.ac.uk (A.E. Bayly).

processing images taken by a digital camera. Ahmed et al. [19] used a cutter blade to manually spread a small heap of powder. The presence of empty patches is extracted from SEM images of a spread powder layer, where particles are immobilised by an adhesive spray. Particle-scale characterisation of a deposited powder layer and direct observation of spreading, however, is challenging due to the lack of transparency of the spreading rig and small particle size, making it difficult to track the motion of individual particle [21,22]. *In situ* observation using high-speed high-energy x-ray imaging has been reported but it is at present limited to dynamics of free surface flow in front of spreading blade [22,23]. Most importantly, there is a lack of quantitative understanding, as the effects of particle properties are difficult to isolate in powder feedstock. In view of these inherent limitations of experimental approaches, discrete element modelling (DEM) has shown great potential to understand powder spreading from the particle scale, as it allows interparticle forces of various sources to be explicitly considered and the resulting packing structure to be readily characterised. Application of DEM has revealed that layer homogeneity is affected by both powder properties (such as, particle cohesiveness [21,24,25], sliding friction [21], particle shape [26,27], size [24] and its distribution [28]) and process parameters (such as, spreading speed [26,29,30], blade clearance [21,31] and blade type [25,26,29,30,32,33]). DEM is also helpful to understand physics underlying powder spreading [31,34]. Nan et al. [31] attributed the presence of empty patches to the occurrence of transient jamming in front of the blade. Recently, Fouda and Bayly [34] applied DEM to benchmark the behaviour of non-cohesive spherical particles. The reduction of packing density in a deposited powder layer compared to the heap in front of the blade was attributed to three major mechanisms: shear-induced dilation, particle rearrangement in the blade gap and particle inertia. To date, few DEM studies have been dedicated to the role of particle cohesion, despite particle cohesion presents a strong impact on the spreading behaviour and subsequently uniformity of the deposited layer [21,24,25,28]. Chen et al. [21] showed that increasing particle cohesion leads to an increased dynamic angle of repose in front of spreading blade and a reduced continuity of powder flow during spreading. Meier et al. [24] found that increasing particle cohesion leads to a decreased packing density but an increased surface roughness. The same conclusion was also drawn by Wang et al. [25]. However, different findings were reported regarding the homogeneity of powder bed. Meier et al. [24] reported a decreased layer homogeneity with increasing cohesive forces while Wang et al. [24] found the layer homogeneity first increases and then decreases with particle cohesion. Despite being novel in understanding the spreading process, the layer characteristics and the underlying mechanisms of cohesive fine powder spreading remain not fully understood.

It should also be noted that most DEM studies mentioned above adopted a reduced particle stiffness that is several orders of magnitude smaller than the true physical value. This is because of the unrealistically small timestep required if using the original particle stiffness, making DEM simulations computationally unaffordable. A reduced particle stiffness is thus normally adopted to accelerate DEM calculations. For non-cohesive particles, reduced particle stiffness has little impact on bulk behaviour, if overlap between particles remains small. However, this is not the case for cohesive particles, particle cohesion needs to be scaled with particle stiffness, otherwise more kinetic energy would be dissipated due to an enlarged interparticle overlap. Several scaling laws have been proposed for this purpose, depending on the force models used in DEM modelling [35,36]. For example, in the work of Nan et al. [31], the experimentally measured surface energy (i.e. 9 mJ/m^2) was scaled with particle stiffness from 211 GPa to 2.1 GPa, giving a value of 1.4 mJ/m^2 for use in the spreading simulation. However, our recent study showed that these existing scaling laws cannot preserve the original particle behaviour [37]. In particular, the sliding and rolling resistances are largely underestimated, undermining the predictive capability of DEM and consequently confidence on the results. This is especially the case for powder spreading where enduring contacts dominate the spreading process. Not only is the validity of the existing scaling approaches questionable, but also the previous studies are quite limited in characterising the spread powder layer, primarily focusing on packing density and surface roughness. To the best of our knowledge, little work has been reported to systematically address pore characterises of a spread powder layer, although it directly linked to some key phenomena in additive manufacturing, such as laser absorption, particle sintering and the presence of defects in a fabricated product.

The aim of this study is thus to establish a discrete element modelling framework for the spreading of cohesive fine powders, where GPU (Graphic Processing Unit) computing [38–40] is combined with a novel stiffness scaling methodology [37] to enable a fast and reliable simulation. The characteristics of spread powder layer are qualitatively illustrated and quantitatively evaluated using a recently developed digital-based approach [41]. How the quality of spread powder layer varies with particle cohesion and the underlying mechanisms are systematically addressed. For the first time, particle clustering and pore characteristics of a spread powder layer are revealed. Since this study is mainly focused on the fundamental understanding of the role of particle cohesion in powder spreading, detailed comparisons between modelling and spreading experiments are thus not aimed here. In this work, particle cohesion is quantified via a dimensionless Bond number (*Bo*) which is defined as the ratio of maximum pull-off force between particles to particle gravity.

2. Model description

In the present study, all the simulations were conducted using an in-house GPU-based DEM code (HiPPS). Its predictive capabilities have been demonstrated in many particulate systems, such as particle packing [37,38], compaction [38,42] and particle-fluid systems [39,40]. The DEM approach is thus only briefly outlined here. More details of force models can be found in our previous studies [37].

For a fine particle of radius R_i, mass m_i and moment of inertia I_i, the translational and rotational motions are governed by the Newton's second law of motion. The resulting governing equations can be written as,

$$m_i \frac{d\mathbf{v}_i}{dt} = \sum_j \left(\mathbf{F}_{\mathrm{cn},ij} + \mathbf{F}_{\mathrm{dn},ij} + \mathbf{F}_{\mathrm{ct},ij} + \mathbf{F}_{\mathrm{dt},ij} \right) + \sum_k \mathbf{F}_{\mathrm{v},ik} + m_i \mathbf{g} \tag{1}$$

$$I_i \frac{d\boldsymbol{\omega}_i}{dt} = \sum_j \left(\mathbf{r}_{ij} \times \mathbf{F}_{\mathrm{t},ij} + \mathbf{T}_{\mathrm{r},ij} \right) \tag{2}$$

where $\mathbf{v}_i$ and $\boldsymbol{\omega}_i$ are the translational and rotational velocities, respectively; $\mathbf{R}_{ij}$ is the vector pointing from the centre of the particle to the contact point with a magnitude of particle radius R_i. $\mathbf{F}_{\mathrm{cn},ij}$, $\mathbf{F}_{\mathrm{dn},ij}$ and $\mathbf{F}_{\mathrm{v},ik}$ are the normal contact force, normal damping force and van der Waals force, respectively. $\mathbf{F}_{\mathrm{ct},ij}$ and $\mathbf{F}_{\mathrm{dt},ij}$ are the frictional force and the damping force in the tangential direction. The torques acting on the particle consists of a torque due to the tangential forces (i.e. the first term on the right side of Eq. (2)) and a rolling resistance torque due to the asymmetric distribution of the contact pressure, given as,

$$\mathbf{T}_{\mathrm{r},ij} = \mu_{\mathrm{r}} \left| \mathbf{F}_{\mathrm{cn},ij} \right| \boldsymbol{\omega}_i / \left| \boldsymbol{\omega}_i \right| \tag{3}$$

where μ_{r} is the rolling friction coefficient.

Normal contact between two particles is assumed to be viscoelastic while tangential contact force is governed by the Mindlin and Deresiewicz theory [43]. The normal and tangential force models are written as,

$$\mathbf{F}_{\mathrm{n},ij} = \frac{4}{3} E^* R^{*1/2} \delta_{\mathrm{n}}^{3/2} \hat{\mathbf{n}} + 2\sqrt{\frac{5}{6}} \beta_{\mathrm{n}} \sqrt{S_{\mathrm{n}} m^*} \mathbf{v}_{ij}^{\mathrm{n}} \tag{4}$$

$$\mathbf{F}_{\mathrm{t},ij} = \begin{cases} -\mu_{\mathrm{t}}|\mathbf{F}_{\mathrm{cn},ij}|\left[1-\left(1-|\boldsymbol{\delta}_{\mathrm{t}}|/\delta_{\mathrm{t,max}}\right)^{3/2}\right]\widehat{\boldsymbol{\delta}}_{\mathrm{t}}+2\sqrt{\tfrac{5}{6}}\beta_{\mathrm{t}}\sqrt{S_{\mathrm{t}}m^*}\,\mathbf{v}_{ij}^{\mathrm{t}} & |\boldsymbol{\delta}_{\mathrm{t}}|<\delta_{\mathrm{t,max}} \\ -\mu_{\mathrm{t}}|\mathbf{F}_{\mathrm{cn},ij}|\widehat{\mathbf{v}}_{\mathrm{t}} & |\boldsymbol{\delta}_{\mathrm{t}}|\geq\delta_{\mathrm{t,max}} \end{cases}$$

(5)

The normal contact force $\mathbf{F}_{\mathrm{cn},ij}$ (i.e. the first term on the right side of Eq. (4)) acts in the normal direction $\widehat{\mathbf{n}}$ pointing from the centre of particle i to that of the particle j, which is a function of the normal overlap, δ_{n}, between two contacted particles. $E^* = E_i E_j/(E_i+E_j)$ is the effective elastic modulus with $E_i = Y_i/\left(1+\nu_i^2\right)$. Y is particle Young's modulus and ν is Poisson's ratio. $R^* = R_i R_j/(R_i+R_j)$ is the effective radius and $m^* = m_i m_j/(m_i+m_j)$ is the effective mass. The normal damping force $\mathbf{F}_{\mathrm{dn},ij}$ (i.e. the second term on the right side of Eq. (4)) is responsible for energy dissipation due to inelastic collisions, in which $S_{\mathrm{n}} = 2E^*\sqrt{R^*\delta_{\mathrm{n}}}$ and β_{n} is the normal damping coefficient. μ_{t} is the coulomb friction coefficient. $\boldsymbol{\delta}_{\mathrm{t}}$ is the particle displacement in the tangential direction and $\widehat{\boldsymbol{\delta}}_{\mathrm{t}} = \boldsymbol{\delta}_{\mathrm{t}}/|\boldsymbol{\delta}_{\mathrm{t}}|$. $\widehat{\mathbf{v}}_{\mathrm{t}} = \mathbf{v}_{\mathrm{t}}/|\mathbf{v}_{\mathrm{t}}|$ is the unit vector of the relative velocity in the tangential direction. $\delta_{\mathrm{t,max}} = \mu_{\mathrm{t}}\delta_{\mathrm{n}}(2-\nu)/(2-2\nu)$ and β_{t} is the tangential damping coefficient. $S_{\mathrm{t}} = 8G^*\sqrt{R^*\delta_{\mathrm{n}}}$, where $G^* = G_i G_j/(G_i+G_j)$ the effective shear modulus, with $G_i = Y_i/2(2-\nu_i)(1+\nu_i)$.

The van der Waals force between two spherical particles follows the Hamaker theory [44], given by,

$$\mathbf{F}_{v,ik} = \begin{cases} \dfrac{AR^*}{6s_{min}^2}\widehat{\mathbf{n}} & s < s_{min} \\ \dfrac{AR^*}{6s^2}\widehat{\mathbf{n}} & s_{min} \leq s \leq s_{max} \\ 0 & s \geq s_{max} \end{cases}$$

(6)

where A is the Hamaker constant. s is the interparticle separation distance and calculated as $s = |\mathbf{r}_i - \mathbf{r}_j| - (R_i + R_j)$.

A newly proposed stiffness scaling methodology [37] is adopted here to accelerate the spreading simulations of cohesive fine powders. Although it is a general practice to use reduced particle stiffness to accelerate DEM simulations; however, our recent study [37] showed that, for cohesive particles, there are many cases where the previously proposed scaling laws fail to preserve original particle behaviour, especially for contact-dominated systems, leading to under-predicted sliding and rolling resistances and a poorly resolved non-contact van der Waals interaction [37]. Different from the existing scaling approaches [36,45], the new scaling methodology consists of three key components: an established scaling law for contact adhesion (i.e. Eq. (7)), a modified normal contact force for the calculation of sliding and rolling resistances (i.e. Eq. (8)) and a new prediction-correction scheme for the estimation of non-contact van der Waals force (i.e. Eq. (9)), as summarised below,

$$\frac{A^R}{A^O} = \left(\frac{Y^R}{Y^O}\right)^{2/5}$$

(7)

$$\mathbf{F}_{\mathrm{cn}}^M = \mathbf{F}_{\mathrm{cn}}^R + \mathbf{F}_{\mathrm{v}}^R - \mathbf{F}_{\mathrm{v}}^O$$

(8)

$$\mathbf{F}_{\mathrm{v,non-contact}} = \sum_k \frac{m_i\left(v_{i,\mathrm{n}} - v_{i0,\mathrm{n}}\right)\widehat{\mathbf{n}}_{ik}}{\Delta t_{\mathrm{DEM}}}$$

(9)

The superscripts R indicates a reduced particle property while O refers to the original particle property. $\mathbf{F}_{\mathrm{cn}}^M$ is the modified normal contact force, $\mathbf{F}_{\mathrm{v}}^R$ and $\mathbf{F}_{\mathrm{v}}^O$ are the van der Waals forces calculated by the reduced and the original Hamaker constant, respectively. This modified calculation of sliding and rolling resistances assumes that transient response of normal contact force has little influence on the bulk behaviour of a contact-dominated system, as it dies out quickly due to viscous damping. Δt_{DEM} is the timestep used in the DEM calculation. $v_{i0,\mathrm{n}}$ is the predicted velocity without accounting for the van der Waals interaction when two particles are not in contact while $v_{i,\mathrm{n}}$ is the corrected velocity when this non-contact van der Waals interaction is considered. Detailed calculation of the corrected velocity and discussion on the applicability of this approach can be found in [37].

3. Simulation conditions and data sampling

Simulations were conducted in a rectangular box with dimensions $40d_{\mathrm{p}} \times 600d_{\mathrm{p}}$, d_{p} is the particle diameter. The model configurations are illustrated in Fig. 1, which represents a generic powder spreading system, comprising a rigid spreading blade and a flat base substrate. Periodic boundary conditions are applied to the front and rear directions of the rectangular box (i.e. horizontal y direction as shown in Fig. 1) to eliminate the so-called wall effects. Idealized mono-sized spherical particles are used here, as spherical shape are typical for particles produced by gas or plasma atomization [24,46]. For simplicity, a typical

Table 1
Parameters used in the present simulations.

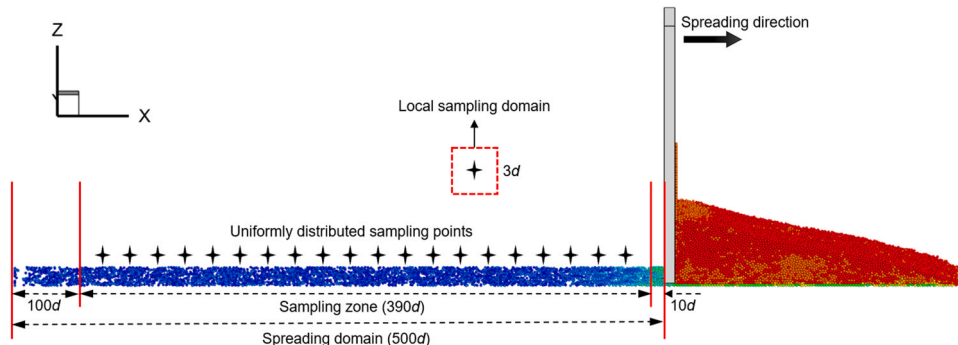| Parameter	Value
Number of particles	100,000
Particle diameter, $d_{\mathrm{p}}(\mu\mathrm{m})$	50
Density, $\rho(\mathrm{kg/m^3})$	4430
Young's modulus, $E(\mathrm{GPa})$	110
Poisson's ratio, ν	0.3
Coefficient of sliding friction, μ_{t}	0.3
Coefficient of rolling friction, μ_r	0.01
Coefficient of restitution, e	0.4
Minimum cut-off distance, $s_{\mathrm{min}}(\mathrm{m})$	1.65×10^{-10}
Blade clearance, $h_{\mathrm{b}}(d_{\mathrm{p}})$	1.5
Blade thickness, $\delta_{\mathrm{b}}(d_{\mathrm{p}})$	4
Blade speed, $v_{\mathrm{b}}(\mathrm{mm/s})$	50

Fig. 1. Schematics of the modelling configuration and the sampling zone of the spread powder bed.
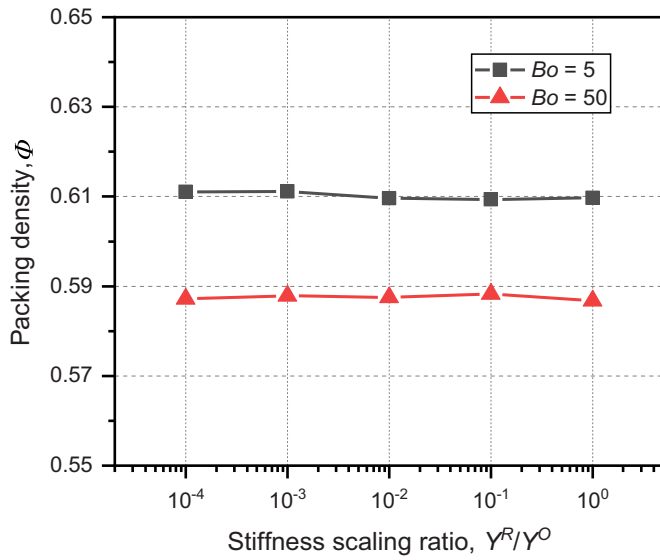
Fig. 2. Effect of stiffness scaling on global packing density for different Bond numbers.

viscoelastic and adhesive contact force model is used here, which can be further improved by introducing more realistic force models, for example, considering plastic deformation [47] and particle sintering [48].

One complete simulation consists of three stages: die filling, heaping, and spreading. At the stage of die filling, a rigid vertical gate is placed $40d_p$ in front of the blade, forming a confined space with a base area of $40d_p \times 40d_p$. First, particles were randomly generated within this confined space without initial overlaps and velocities. Secondly, particles were settled under the effect of gravity until forming a stable packing. At the heaping stage, the front gate was removed, which allows a stable heap to be formed in front of the blade. Finally, for the stage of

spreading, the blade was lifted up to create a fixed blade clearance (i.e. $1.5d_p$) and was translated at a constant velocity in the positive x direction, allowing particles to be deposited on the base substrate.

Particle properties are those typical of Ti-6Al-4V powder, following that used by Meier et al. [24]. The modelling parameters are summarised in Table 1. It is assumed that the rigid blade, front gate, and base substrate have the same properties as that of particles. A minimum cut-off distance s_{min} is introduced in the calculation of van der Waals interactions, same as that used in the work of Parteli et al. [49]. A time step of 2×10^{-8} s is used for particles of reduced particle stiffness. Particle cohesion is specified via a dimensionless Bond number (Bo). In the case of van der Waals force, Bond number is defined as,

$$Bo = \frac{F_{v,max}}{mg} = \frac{A}{16\pi R^2 \rho g s_{min}^2} \qquad (10)$$

which is the ratio of the maximum pull-off force to particle gravity. A wide range of particle cohesions are examined here by varying Bo from 0 to 400, which can be justified by the values found in the literature. For example, Bo is around 255 in the work of Nan et al. [31] for 45 μm stainless steel particles and cohesive force is two orders of magnitude larger than particle gravity for a plasma-atomized Ti-6Al-4V powder with a median particle diameter of 17 μm [24].

A total length of $500d_p$ is spread for all the cases considered here. The first $100d_p$ of a spread powder bed and $10d_p$ immediately behind the spreading blade are excluded from data analysis. Data sampling was conducted within a length of $390d_p$, as shown in Fig. 1. A recently developed digital-based approach [41] is adopted to characterise the spread powder layer in term of packing density, surface profile and pore characteristics. The working space is discretised into voxels, with those voxels located within solid particles labelled as solid voxel. To aid data sampling, a Cartesian 2D sampling grid along the base surface is used to sample local properties. As the actual height of powder layer varies with both particle and process parameters and under certain circumstances it may be larger than the blade clearance. A gap-based packing density is thus defined here, which differs from the conventional definition but enables a consistent comparison among different cases and can quantify
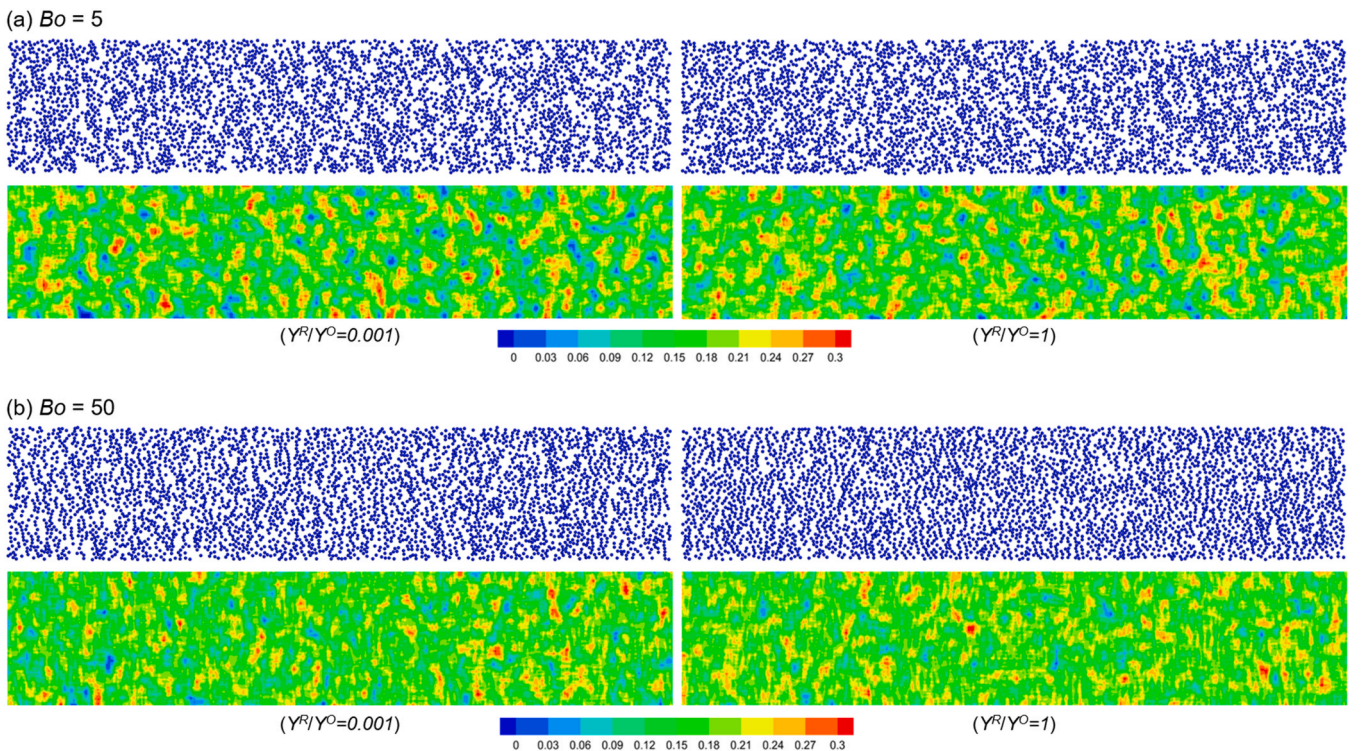

Fig. 3. Top view of spread powder layer and spatial density distribution of different stiffness scaling ratios, in which (a) $Bo = 5$ and (b) $Bo = 50$.

the mass per unit area being deposited on the build plate. The local packing density at each grid node is calculated as a ratio of particle volume to the volume of a sampling domain with a height same as the blade clearance (i.e. h_b),

$$\phi = \frac{1}{s_\Omega^2 h_b} \sum_{ip \in \Omega} V_{ip} \tag{11}$$

where s_Ω represents size of the local sampling domain Ω. The local sampling domain has a parallelepiped shape, with a square base and a dimension of $3.0d_p$. The local packing density is simply calculated as a ratio of the number of solid voxels to the total number of voxels within the local sampling domain. The surface height at each grid node is determined as the maximum vertical coordinate (i.e. z-coordinate) of solid voxels found within the local sampling domain. It is of practical interest to characterise the region which can potentially lead to failure. Therefore, two types of pores are characterised for the spread powder layer, namely the so-called density pore and chamber pore [41]. The density pore is identified by thresholding the spatial distribution of local packing density, which allows us to identify those less populated areas in a spread powder layer. Here, as an example, the density threshold is set to 0.1. The concept of so-called chamber pore is adapted here to quantify the size of empty patches. The size of density pore is defined as its equivalent circular area diameter (i.e. the diameter of a circle of same area as the pore region) while the size of chamber pore is defined as diameter of the largest inscribe circle. Details of the calculation approach can be found in the previous study [41].

4. Validation of stiffness scaling

The validity of using reduced particle stiffness in DEM modelling is examined in both particle packing and spreading. Only two levels of particle cohesion (i.e. $Bo = 5$ and 50) are tested here, due to a high computational demand associated with the case of original particle stiffness. Fig. 2 shows the global packing densities as a function of stiffness scaling ratio for packed beds formed at the die filling stage. The global packing density is calculated as a ratio of solid volume to the volume of space occupied by the particles,

$$\Phi = \frac{1}{L_x L_y (0.9 z_{max} - z_{min})} \sum_{i}^{n} \pi d_i^3 / 6 \tag{12}$$

where L_x and L_y are the box dimension in the horizontal directions (i.e. $40d_p$), respectively. z_{min} and z_{max} are the minimum and maximum co-ordinates of a packed bed in the vertical direction. To reduce variability and surface effect, particles on the free surface of the packed bed are excluded from the calculation. The lower packing density seen with a higher Bo is qualitatively consistent with previous findings, as the interparticle cohesion resists relative motion between particles and hence leads to a loose packing [50,51]. For each Bo, the global packing density remains almost independent of scaling ratio, the variability is within 0.2% of that of the original particle stiffness in both cases, confirming the capability of the present model to achieve a stiffness-independent packing of cohesive fine powders.

The validity of the stiffness scaling approach is further examined in the case of powder spreading. Fig. 3 compares local packing density distributions of the spread powder layer where different scaling ratios are adopted for the calculation. Scaling can be seen to have little influence on the packing density distribution. As shown in Fig. 4, the relative differences between different median local packing densities are $< 3.6\%$ for $Bo = 5$ and $<5.3\%$ for $Bo = 50$. The interquartile ranges are also relatively constant, the relative difference between different scaling is $< 4.5\%$ for a $Bo = 5$ and $<13.7\%$ at $Bo = 50$. This shows that the properties of the spread bed are well maintained when the particle stiffness is reduced by three orders of magnitude. To be computationally efficient, a scaling ratio of 0.001 is adopted in the present study.
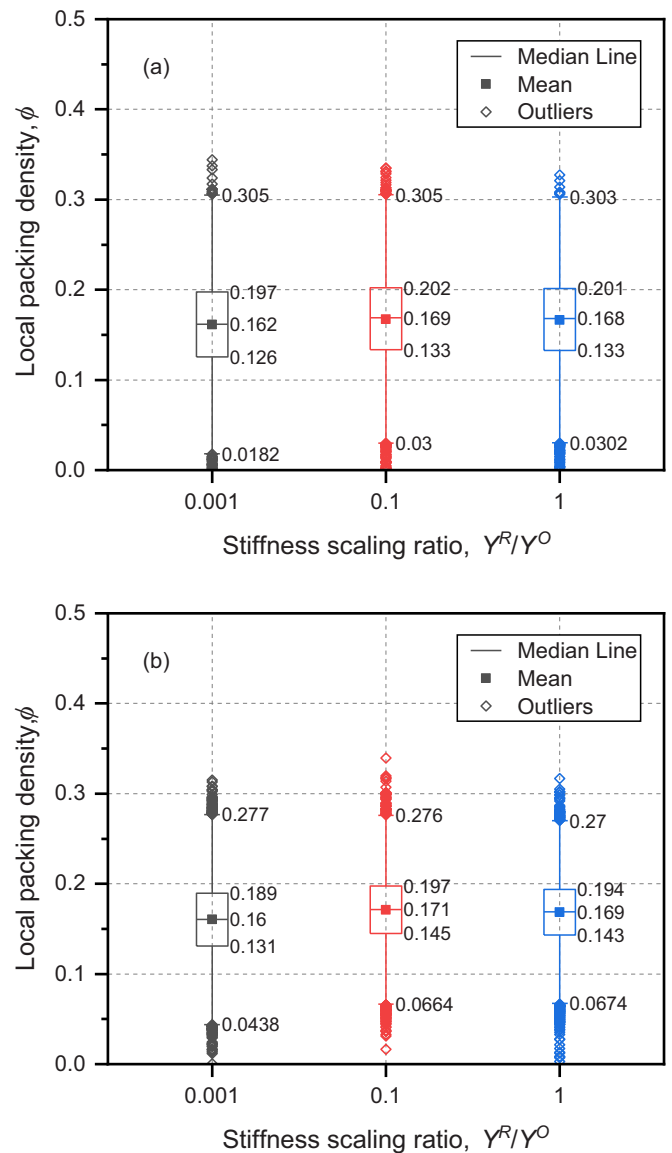

Fig. 4. Box plots comparing the results of local packing density obtained using different scaling ratios, with (a) $Bo = 5$ and (b) $Bo = 50$. The box height is equal to the interquartile range (IQR) which defines the range of the middle 50% of the ranked data. The whiskers indicate the range of data between -1.5IQR and 1.5IQR.

5. Effect of particle cohesion

5.1. Packing structure

Fig. 5 shows the resulting packing structure of spread powder layers affected by particle cohesion. For illustration purposes, only a section of the layer is shown. Particles are coloured by coordination number (CN) (i.e. number of particle-to-particle contacts), where two particles are considered in contact when the distance between two centroids is smaller than a critical value (i.e. $1.005d_p$) [50,51]. Spatial distribution of packing density is also examined, as it reflects the uniformity of mass being deposited on the substrate. Local packing density is sampled using a 2D grid, with a grid size of $1.0d_p$ and a local sampling size of $3.0d_p$ at each grid node.

Particle cohesion is seen to have a significant impact on the resulting packing structure. For non-cohesive particles (i.e. $Bo = 0$), both particle clustering and large empty patches are visible in the powder layer. Local packing densities can reach as high as 0.3, indicating a closely packed
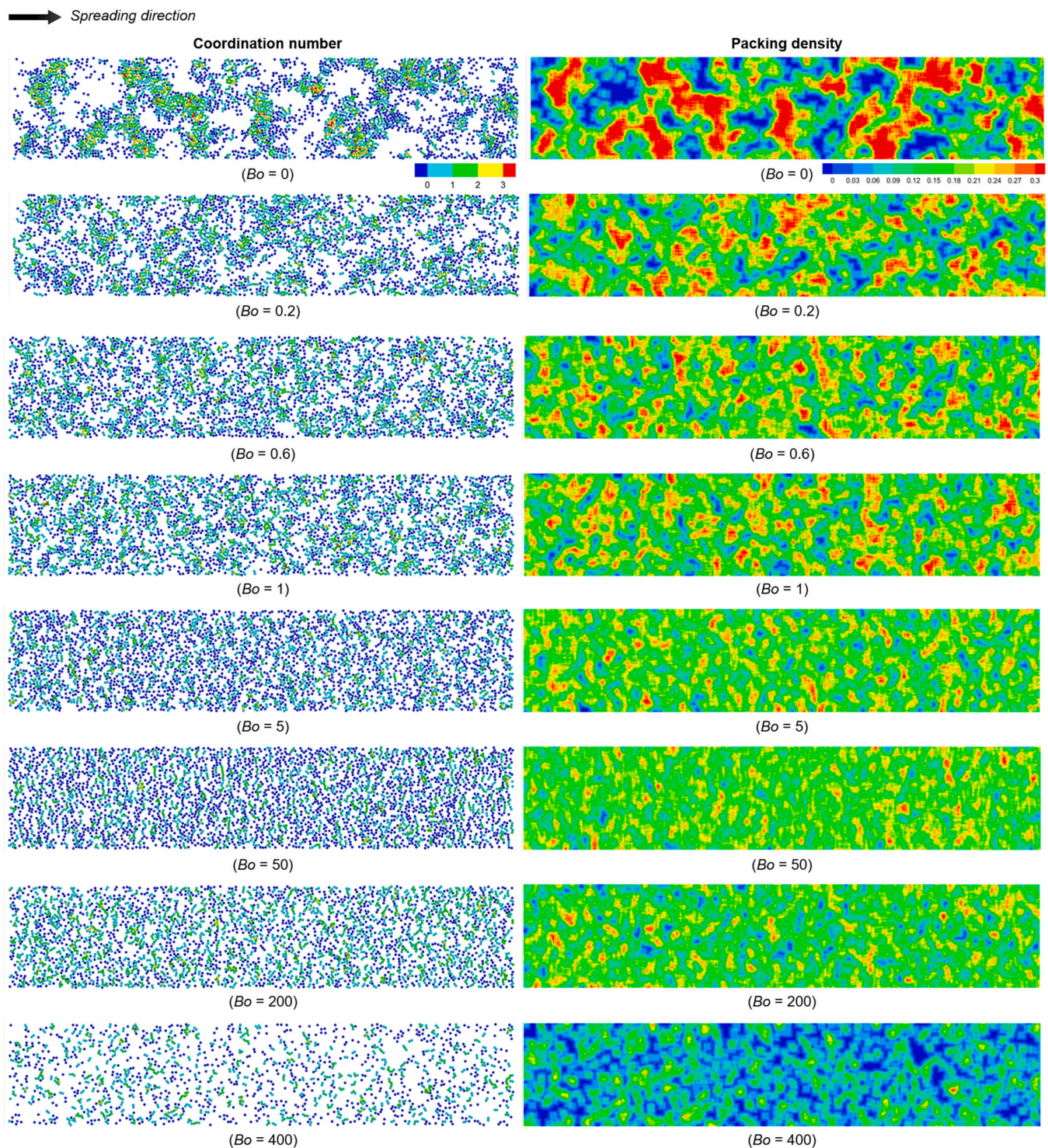
Fig. 5. Top view of spread powder layer and spatial distribution of packing density for different Bond numbers. For the particle view, particles are coloured by coordination number. Animations of the spreading can be found in the supplementary, where particles are coloured velocity in the spreading direction.

structure within these clusters, although it is significantly lower than that of a random close packing (0.62–0.64) due to a dominant mono-layered packing structure. In contrast, no significant variation of packing density can be observed in the spreading direction for cohesive particles. A slight increase of particle cohesion (i.e. $0 < Bo < 5.0$) results in a significant reduction in the degree of particle clustering. The uniformity of the spread layer continues to improve with further increase of Bo up to 50, as evidenced by a further reduction in the size of empty patch and a more homogeneous density distribution. However, a sparser

layer starts to emerge when Bo is beyond 200. It is found that, within this Bo range, particle assembly in front of the blade largely maintain its shape integrity during spreading due to very strong interparticle attractive forces. The deposition process can thus be viewed as particles being stripped off the base of a solid-like assembly by a moving cohesive plate. Consequently, particles being deposited on the substrate are reduced considerably with increasing cohesion. This is different from the previous work [31] where large variation in the size of empty patches is still observable when Bo is larger than 200. For all the cases

considered here, coordination numbers are quite small. This can be related to the dominant mono-layered structure because of a small blade gap (i.e. $1.5d_p$). Moreover, a large proportion of particles has zero particle-to-particle contact, especially at $Bo = 50$. And chain-like structure starts to show when Bo is larger than 1.0 due to the increase of interparticle attractive forces, and consequently leading to a reduction in the coordination number.

Fig. 6 shows the frequency distribution of coordination number in the spread layer. For all the considered cases, coordination number is smaller than 5. For non-cohesive particles, almost 45% of the particles have zero particle-to-particle contact. Particles with a higher CN accounts for a smaller proportion. However, an appreciable ratio of particles with a CN of 4 is still obtained in the spread layer of non-cohesive particles. As shown in Fig. 6(a), for $Bo < 1.0$, the increase of particle cohesion decreases the ratio of free particles (i.e. no contact with other particles) while increases the ratio of particles with one contact. The particles having more than two contacts are less affected. Within this Bo range, particles gain a high level of mobility after being released from the blade gap. The increase of interparticle cohesion makes particles more likely to stick together to form doublet, and thus leading to a decrease in the ratio of free particles and an increase of particles with one contact.

A more complicated behaviour is observed with a higher level of particle cohesion. As shown in Fig. 6(b), the ratio of free particles increases with Bo up to 50 and then drops to a local minimum at $Bo = 200$, beyond which it increases again. However, an opposite trend is observed for particles having contacts. For Bo between 1.0 and 50, this behaviour reflects the presence of two competing mechanisms: collision-induced particle clustering and particle-wall cohesion. Within this Bo range, particle-wall cohesion takes over as the dominant mechanism enhancing layer uniformity while suppressing the form of large clusters. Consequently, the ratio of free particles increases while the ratio of particles having more than one contacts starts to decrease. However, when $Bo > 50$, particles have very limited mobility after being discharged from the blade. The interparticle cohesion becomes so strong that particles contacted with other particles in front of the blade are more likely to stay in contact after being released from the blade gap. Because of the small blade clearance ($1.5d_p$) used in the present study, particles are more likely to form doublet, thus resulting in a significant ratio of particles with a single contact. When Bo is further increased (i.e. $Bo > 200$), a static assembly begins to form in front of the blade due to the large interparticle cohesive force. Particles are less likely to be escaped from the blade clearance, thus leading to an increased ratio of free particles and a decrease in the ratio of particles with contacts.

To view vertical structure of the spread layer, Fig. 7 shows frequency distribution of particle centres in the vertical direction. All the distributions show a significant peak at $0.5d_p$, suggesting a dominant mono-layered packing structure. For $Bo < 1.0$, more than 99% of the particles are touching the base substrate and thus are not shown here. With increasing Bo, particles located within the range of between $0.5d_p$ and $1.2d_p$ start to increase. It is interesting to see that, because of strong interparticle cohesion, there is a small number of particles ($< 5\%$) located above $1.0d_p$ when $Bo > 50$.

Fig. 8(a) shows statistical distribution of local packing density in the spread layer as a function of Bo. The median packing density decreases slightly with Bo up to 200, suggesting a limited influence with this Bo range. However, this is followed by a sharp drop when $Bo > 200$, as less particles being discharged from the blade gap due to the formation of a static assembly. To measure the dispersion of local packing density, Fig. 8(b) shows the ratio of IQR to the median as a function of Bond number, which has a similar role as coefficient of variation (or relative standard deviation) but is more robust to the presence of outliers. A large IQR\Median ratio indicates a high level of data dispersion. The results in Fig. 8(b) indicates the presence of four regimes regarding the variation of IQR\Median ratio, suggesting there are different dominant mechanisms of fine powder spreading. For the cases considered here, a
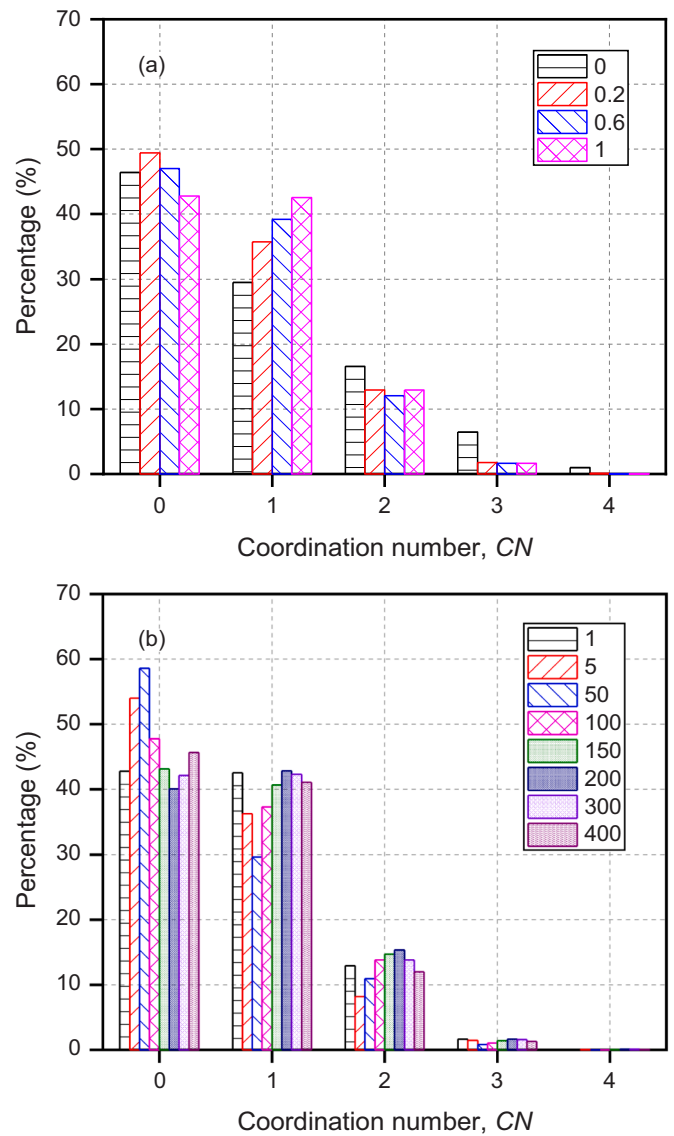

Fig. 6. Probability density distribution of coordination number for different Bond numbers, in which (a) $Bo \leq 1$ and (b) $Bo \geq 1$.
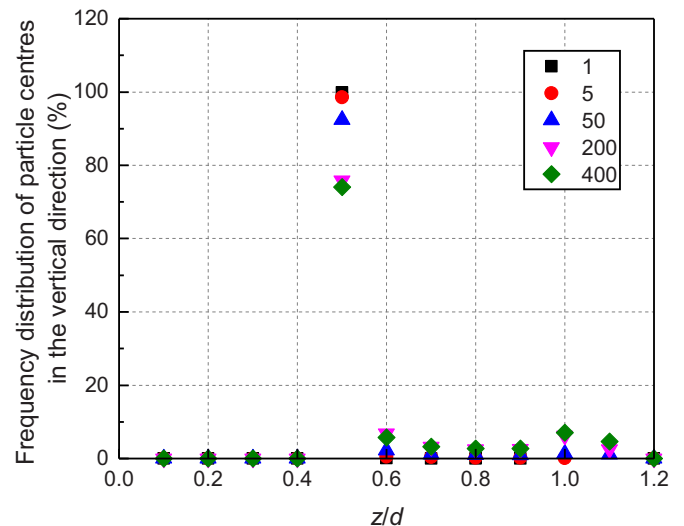

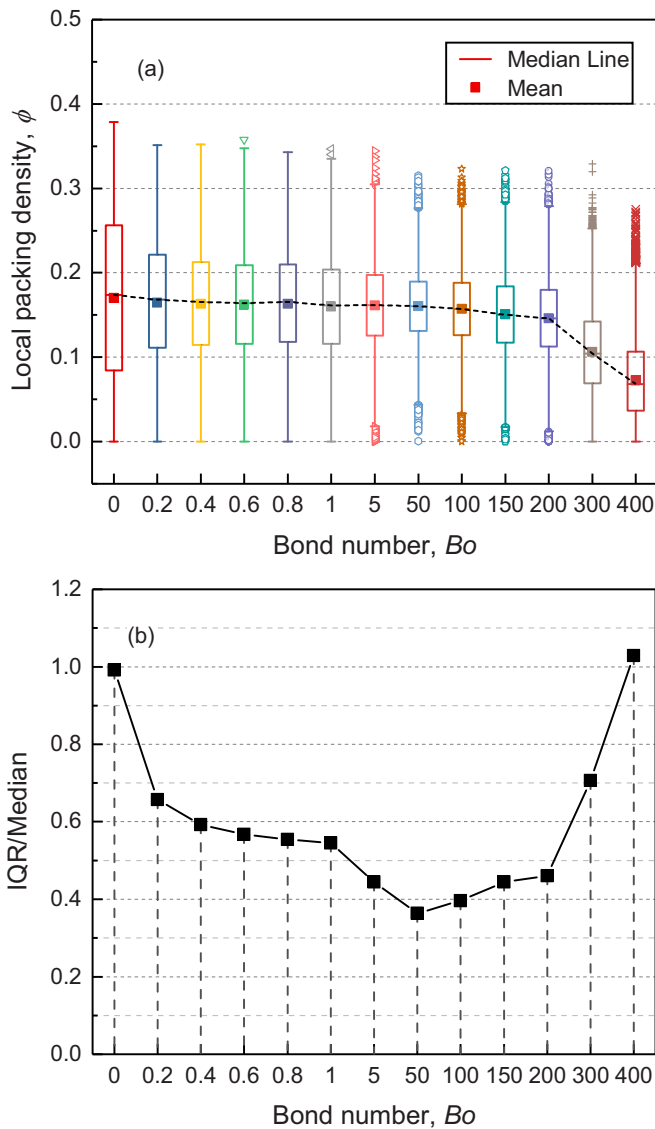**Fig. 7.** Vertical distribution of particle centres within the layer.

Fig. 8. Effect of particle cohesion on (a) the distribution of local packing density and (b) the ratio IQR to median packing density.

local minimum is observed at $Bo = 50$ while both weak (i.e. $Bo < 0.2$) and strong cohesion (i.e. $Bo > 200$) lead to reduced layer homogeneity.

5.2. Particle clustering

Particle clustering or agglomeration is a pronounced feature of cohesive particulate systems. However, the degree of particle clustering has not been addressed before in a spread powder bed, despite its important practical consequences in additive manufacturing. For example, its presence has an impact on the absorption of laser energy, heat transfer and mass transfer during melting. Fig. 9 illustrates the presence of particle clusters in the spread layer, with each coloured by its orientation relative to the spreading direction. For clarity, particles without contacting with other particles (i.e. single particle) are not shown here. Cluster size is seen to decrease significantly with Bo up to $Bo = 5.0$ and then increases slightly with further increase of Bo. Here, the cluster size is defined as the number of particles consisting it. The shape of the cluster is also affected, shifting from large agglomerates to chain-like structures. Chain-like structure is seen to dominant when $Bo > 5$ and most clusters are found in the form of doublet. Cluster orientation also shows a dependence on particle cohesion. Clusters for a
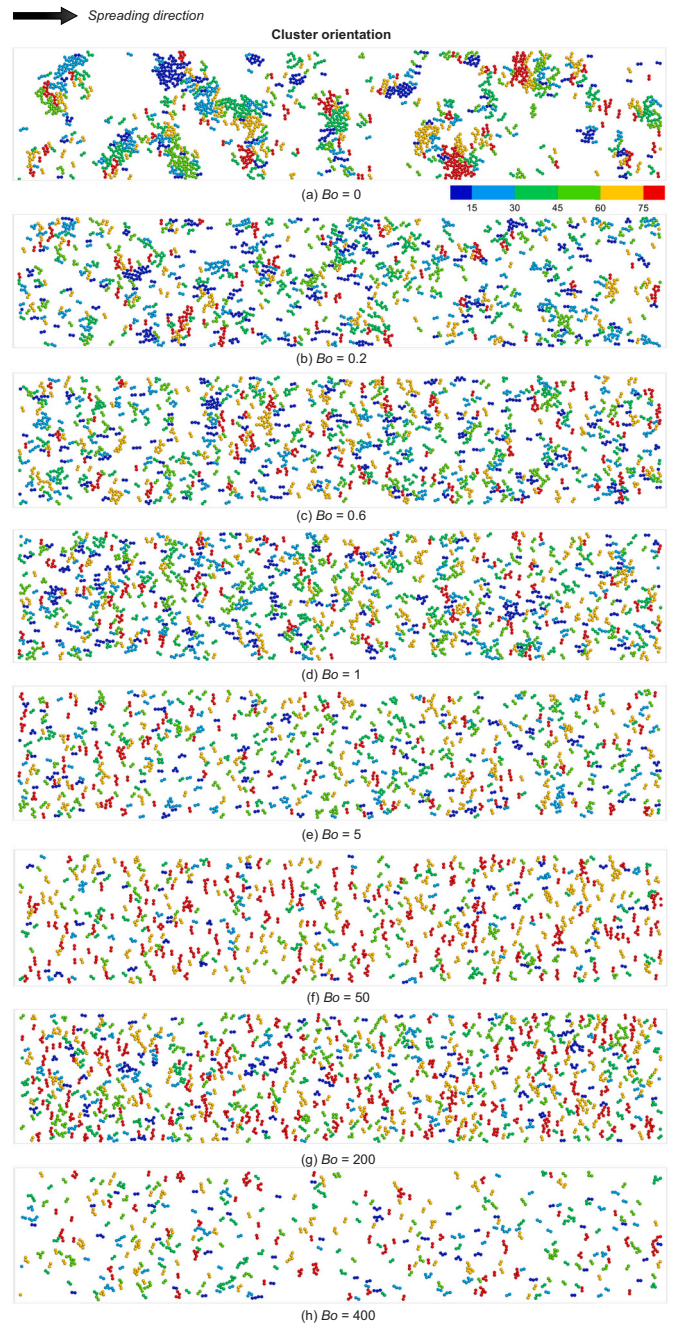

Fig. 9. Particle clusters in the spread powder layer for different Bond numbers, in which (a) $Bo = 0$, (b) $Bo = 0.2$, (c) $Bo = 0.6$, (d) $Bo = 1$, (e) $Bo = 5$, (f) $Bo = 50$, (g) $Bo = 200$ and (h) $Bo = 400$. Particles are coloured by the orientation of the cluster relative to the spreading direction.

Bo between 5 and 200 shows a preferred orientation perpendicular to the spreading direction while clusters in other cases are more randomly orientated.

To quantitatively evaluate the extent of particle clustering, particle-based frequency distribution of cluster size is presented in Fig. 10. Most clusters are found in the form of doublet, partly due to the small blade clearance adopted here (i.e. $1.5d_p$). For non-cohesive particles, the cluster size can reach as large as 136. For weakly cohesive particles (i.e. $Bo \leq 1$), as shown in Fig. 10(a), the ratio increases with Bo for small clusters (i.e. < 4) while drops for larger clusters (i.e. > 8). This clearly shows that the presence of particle cohesion can suppress the formation of large agglomerates. For moderately cohesive particles (i.e. $Bo \leq 50$), clustering is further suppressed with increasing particle cohesion. More
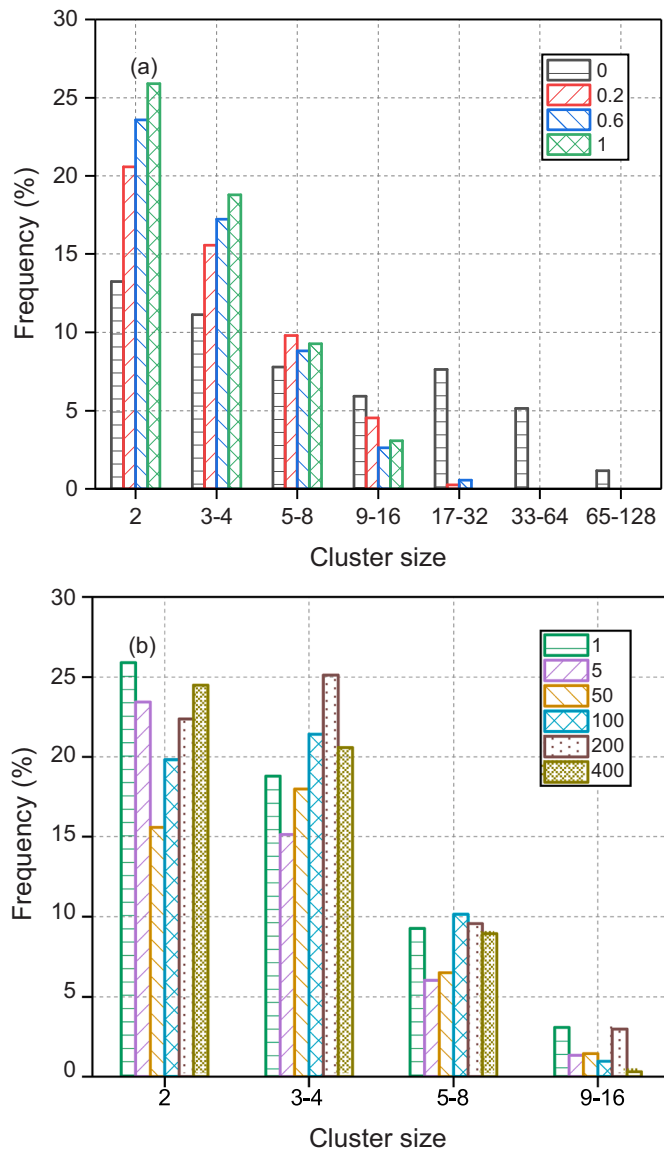
Fig. 10. Frequency distribution of particle-based cluster size in the spread layer, in which (a) Bo $\leq$ 1 and (b) Bo $\geq$ 1.

than 95% of the particles form a cluster with a size smaller than 9. However, the clustering ratio increases again when Bo $\geq$ 50. It is found that, within this Bo range, particles tend to be adhered to the substrate immediately after being discharged from the blade gap, as the increase of particle cohesion leads to higher particle-wall adhesion. At the same time, the interparticle attractive force is significantly enhanced, making particles more likely to maintain their contact status after being deposited on the substrate and thus promoting the formation of chain-like structured cluster. Because of the small blade clearance, chain-like structure is still the dominant form. For larger clusters (i.e. > 2), a further decrease of the clustering ratio can be observed for strongly cohesive particles (i.e. Bo $\geq$ 200). This is because interparticle attractive force becomes so strong that a static particle assembly formed in front of the blade, hindering the release of particles, and consequently reducing the formation of large clusters.

Fig. 11 shows the particle-based orientation distribution of clusters in the spread powder layer. Here, clusters are classified into three groups: small cluster with a size of 2, medium cluster with a size of 3 or 4 and large clusters with a size larger than 5, to examine the correlation between cluster size and its orientation. As shown in Fig. 11(a), clusters of non-cohesive particles have no orientation preference, irrespective of the cluster sizes. For weakly cohesive particles (i.e. $Bo \leq 1.0$), small clusters (doublets) tend to align in the spreading direction while no preferential alignment is observed for medium and large clusters. The increase of particle cohesion slightly increases the clustering ratio of doublets while not affecting much their orientations. In contrast, as shown in Fig. 11(b), clusters are more likely to be aligned perpendicular to the spreading direction when particle cohesion is further enhanced. It is especially the case when $Bo \geq 50$. This again can be explained as the loss of mobility after particles being discharged and the increase of interparticle attractive forces. Consequently, small clusters and clusters that are aligned with the blade have a higher survival rate when escaping from the blade gap. Large clusters and clusters with other orientations are more likely to be disintegrated by transient jamming that occurs in front of the blade. However, for strongly cohesive particles (i.e. Bo > 200), large interparticle attractive force leads to the formation of a rigid assembly, and thus reducing particles being discharged and increasing the survival rates of clusters with other orientations, as particles are essentially being stripped off the base of the assembly. That is why the orientation of clusters is slightly more random at $Bo = 400$ compared to that of $Bo = 200$. Since large clusters are more difficult to survive compared to small clusters, the clusters with random orientations are dominated by the form of doublet.

5.3. Surface profile

Fig. 12 shows the effect of particle cohesion on the surface profile of a spread powder layer, where surface height is sampled with the aid of a 2D grid, where the grid size is set to $1.0d_p$ and a local sampling size of $1.0d_p$ is used. For weakly cohesive particles (i.e. Bo $\leq$ 1.0), more than 80% of the spread powder layer has a surface height between $0.75d_p$ and $1.0d_p$, indicating a mono-layered packing structure. In contrast, multiple layered structure starts to emerge when $Bo \geq 5$. The value of zero corresponds to those empty patches observed in Fig. 5. Its ratio decreases with particle cohesion up to $Bo = 50$, beyond which it increases again. For cohesive particles, the surface height can be larger than $1.25d_p$ but is still limited by the blade clearance (i.e. $1.5d_p$). The ratio for $0.75d_p < z_{ij} \leq 1.0d_p$ decreases with particle cohesion while the ratio for $z_{ij} > 1.0d_p$ first increases up to $Bo = 50$ and then decreases.

To quantify the effect of particle cohesion on the surface profile, surface roughness (Ra) is presented in Fig. 13 as a function of Bo, which is calculated as arithmetical mean deviation of the surface height. A smaller value of Ra indicates a better surface homogeneity. Variation of surface roughness is found to be consistent with the distribution of local packing density (i.e. Fig. 8(b)), where four different regimes can also be observed. For weakly cohesive particles (i.e. Bo $\leq$ 1), surface homogeneity increases with particle cohesion, approaching a value around $0.12d_p$. With further increase of particle cohesion, a local minimum is seen at $Bo = 50$, beyond which Ra increases with Bo at a decreasing rate up to $Bo = 200$. For strongly cohesive particles (i.e. $Bo > 200$), Ra increases almost linearly with Bo. This is different from the observations of Wang et al. [25] where the surface roughness was found to increase with Hamaker constant.
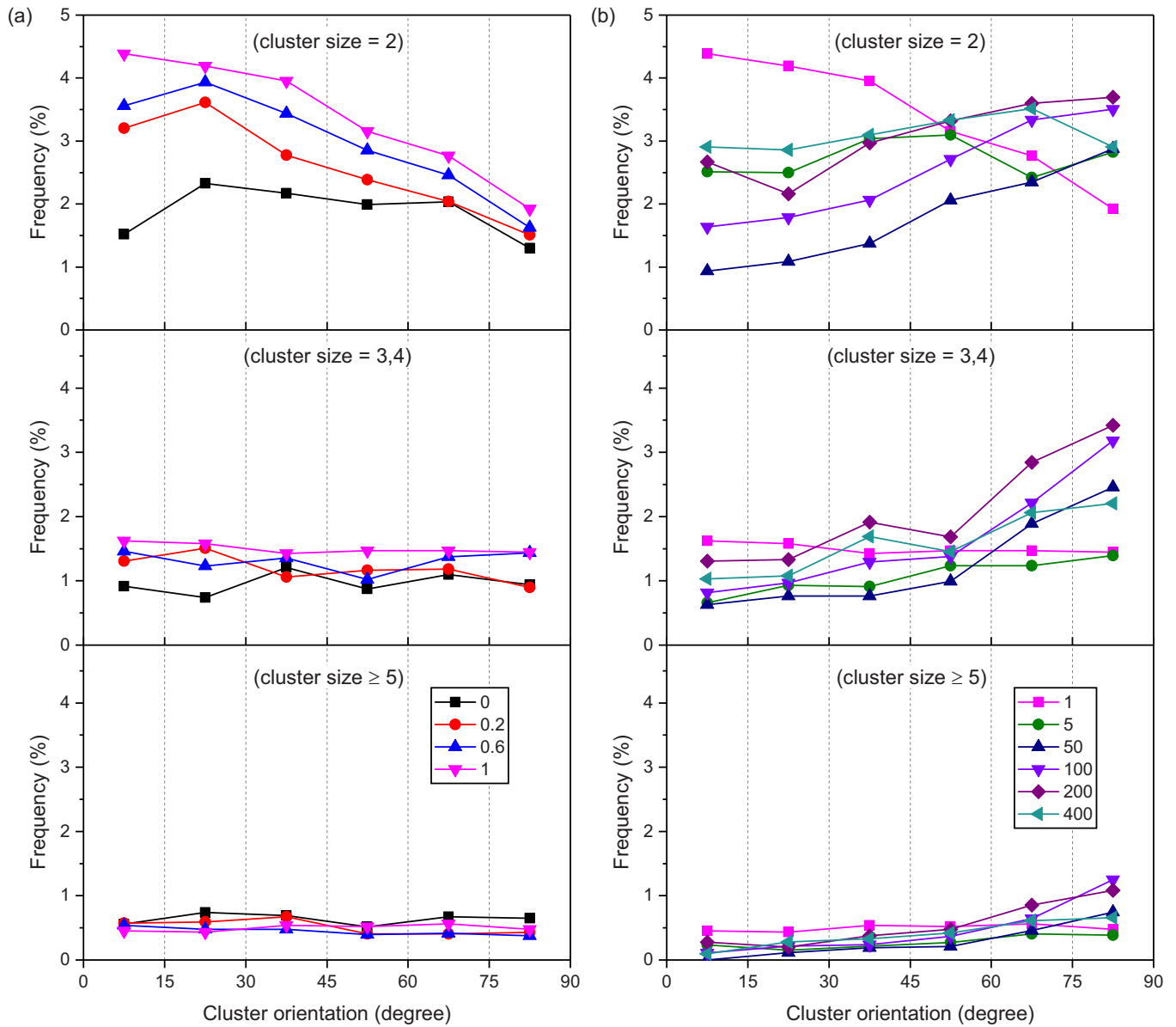
Fig. 11. Frequency distribution of cluster orientation in the spread powder layer, in which (a) Bo ≤ 1 and (b) Bo ≥ 1.

5.4. Pore characterization

As shown in Fig. 14, for weakly cohesive powders (i.e. $Bo < 1$), density pore tends to have an irregular shape and possesses a rather random orientation. With increasing particle cohesion, the resulting pore becomes more elongated and aligns more perpendicular to the spreading direction. The number of pores and the corresponding pore size are also affected. The density pore size first decreases until $Bo = 50$ and then increases with particle cohesion. An opposite trend is observed for the number of density pores. At $Bo = 400$, a single large pore that covers most of the spread powder layer is obtained, corresponding to a very sparse particle distribution. Like that of the density pores, the size of chamber pore is also seen a decrease followed by an increase with Bo. For cohesive powders, chamber pores are distributed quite uniformly,

with no clear localization observed in the spreading direction while large size variations of the chamber pore can be observed in the spread layer of non-cohesive particles.

A quantitative description of the role of particle cohesion can be revealed by the cumulative distribution of pore size, as shown in Fig. 15. For non-cohesive particles, the size of density pore can reach $24d_p$, which is significantly larger than those of cohesive particles. The slope of distribution first increases and then decreases with particle cohesion, peaking at $Bo = 50$. For the weakly cohesive powders ($Bo < 1$), a significant increase of the slope can be observed, suggesting a slight addition of particle cohesion can significantly reduce the pore size. Consistent with the distributions of density pore, the slope of the distribution of chamber pore also peaks at $Bo = 50$. For $Bo < 200$, most of the chamber pores are smaller than $4.0d_p$ and the distributions almost
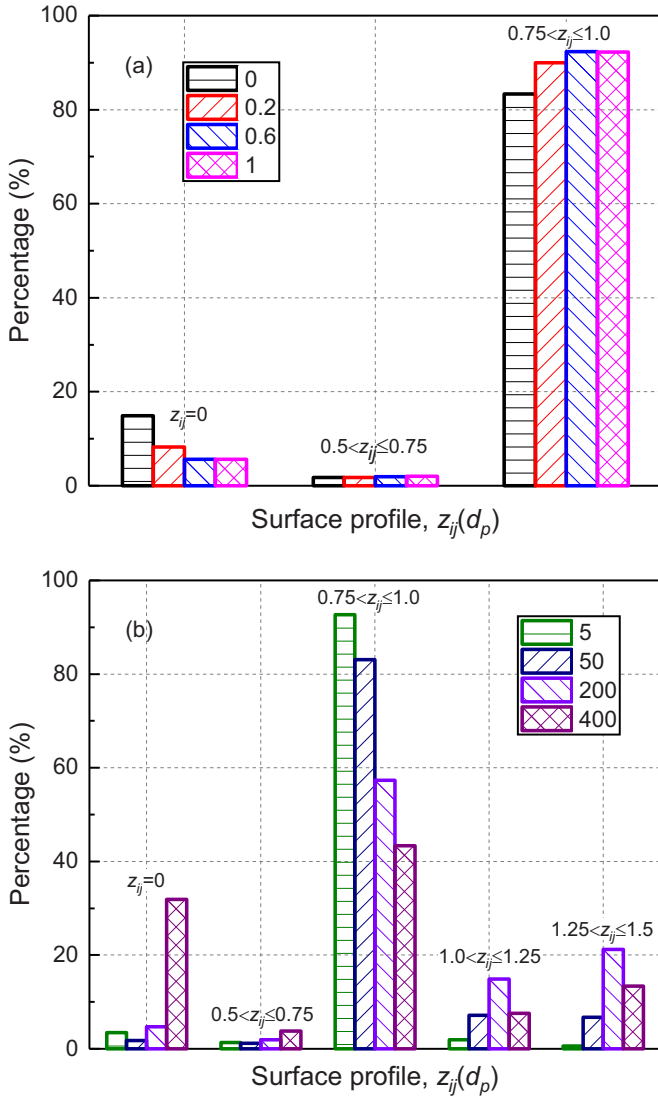
Fig. 13. Effect of particle cohesion on surface roughness of a spread powder layer.

Fig. 12. Effect of particle cohesion on the distribution of surface height of a spread powder layer, in which (a) $Bo \leq 1$ and (b) $Bo \geq 1$.

follow a same trend till a pore size of $1.0d_p$, indicating a limited influence of particle cohesion on the ratio of small chamber pores.

To further explore the role of particle cohesion, both types of pores are classified into six size groups. As shown in Fig. 16(a), the increase of particle cohesion in the range of $Bo \leq 1$ mainly reduces the ratio of large pores ($>5d_p$) while further increase of the particle cohesion leads to a change of the dominant small pore size, from $2d_p$ to $3d_p$ for $Bo = 5$, to $1d_p$–$2d_p$ for $Bo = 50$ and back to $2d_p$–$3d_p$ for $Bo = 100$. For $Bo \geq 200$, the spread layer is again dominated by large pores ($>5d_p$). For the chamber pores, as shown in Fig. 16(b), the groups of large pores ($>3d_p$) follow a same trend that increasing particle cohesion leads to a decrease followed by an increase of the ratio. The very small chamber pores ($<1.0d_p$) remains relatively stable up to $Bo = 50$, beyond which pores smaller than $2d_p$ are seen a sharp drop in the ratio. In contract, variation of the medium sized chamber pores ($2d_p$–$3d_p$) is more sensitive to particle cohesion, indicating a dependence that is in line with other descriptors discussed before.

5.5. Mechanisms affecting powder spreading

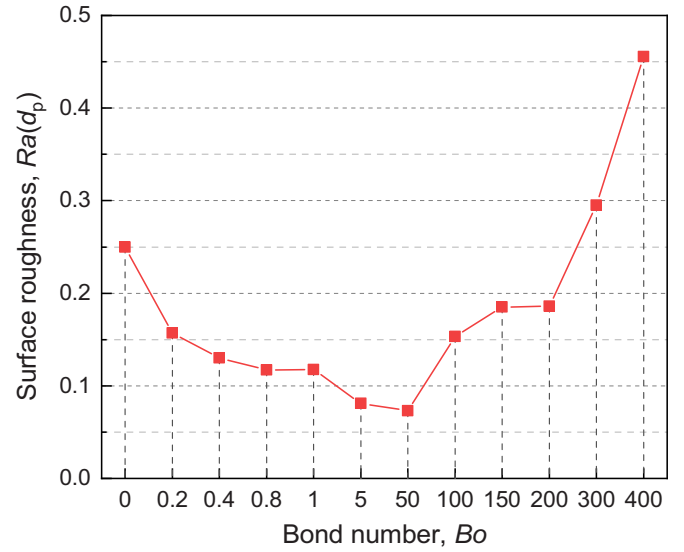In terms of the mechanisms underlying inhomogeneous particle distribution, it can be understood from the competing effects of particle mobility, particle-particle, and particle-wall cohesions. Animations of the spreading process can be found in the supplementary, in which particles are coloured by the velocity in the spreading direction. After being released from the blade clearance, particles gain a momentum to continue moving forward. The resistances to particle's motion are mainly composed of sliding and rolling resistances. Compared to rolling, sliding is the dominant mode of motion for a cohesive particle. A dimensionless inertial length, I_μ, characterising the distance that a particle can travel before friction brings to a stop can be estimated as,

$$I_\mu = \frac{mV_s^2}{2\mu_t(mg + F_v)d_p} = \frac{V_s^2}{2\mu_t g d_p(1 + Bo)} \tag{13}$$

where V_s is the blade speed which is characteristic of the particle velocity immediately after being released from the blade gap. μ_t is the sliding friction coefficient. F_v is the pull-off force required to separate a particles from the base substrate. The $\mu_t(mg + F_v)$ denominator is an estimate of the frictional force on the particle once it has left the blade gap. If particle-particle and particle-wall sliding friction coefficients are different, this term can be adjusted, and a modified inertial length can be defined.

The dimensionless inertial length, I_μ, is 8.49 for non-cohesive particles and 4.24 when $Bo = 1.0$. Within this Bo range (i.e. $Bo \leq 1$), particles gain a high level of mobility after being discharged from the blade gap. They continue to move forward and collide with each other, dissipating kinetic energy and consequently leading to the formation of large clusters. Collision-induced energy dissipation can be thus attributed as the dominant mechanism responsible for the inhomogeneity of a spread powder layer, which is also one of the mechanisms giving rise to particle clustering in gas-solid fluidization [52]. For weakly cohesive particles (i. e. $Bo \leq 1$), the increase of particle cohesion mainly reduces the cluster size and thus leading to an improved layer homogeneity.

When particle cohesion becomes more significant, I_μ quickly drops to 1.41 for $Bo = 5.0$ and 0.16 for $Bo = 50$. Particles have very limited mobility within this range of Bo. Particles adhere to the substrate shortly after being released from the blade gap. Collision-induced particle clustering is thus significantly suppressed. Particle-wall adhesion takes over as the dominant mechanism which can enhance the uniformity of a spread layer. Further increase of particle cohesion (i.e. $50 < Bo \leq 200$), I_μ drops to 0.04 at $Bo = 200$. Particles adhere to the base substrate immediately after being released from the blade gap. Chain-like cluster structure starts to dominate in the spread powder layer, which can be
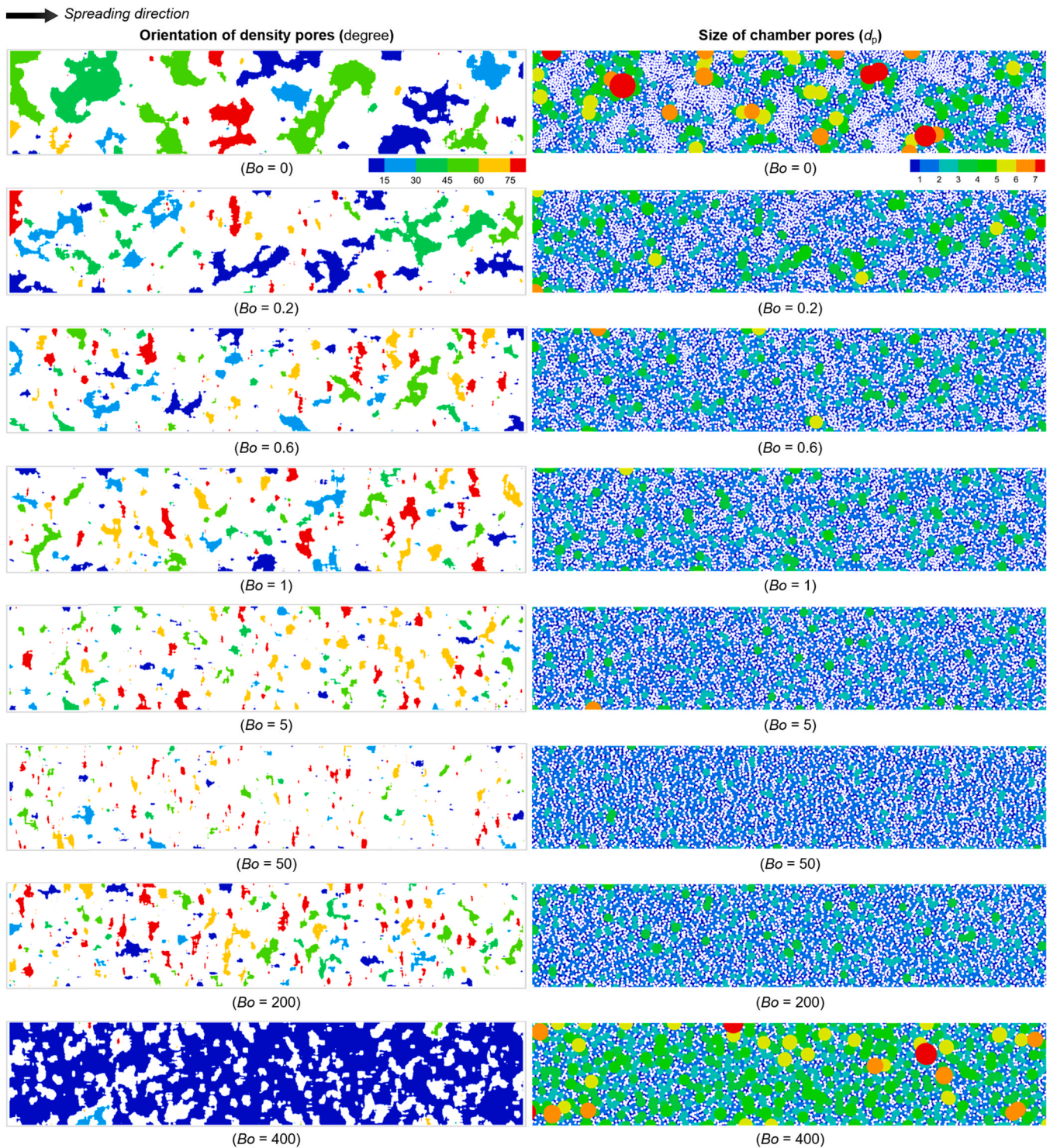
Spreading direction

Orientation of density pores (degree)

Size of chamber pores (d_p)

(Bo = 0)

15 30 45 60 75

(Bo = 0)

1 2 3 4 5 6 7

(Bo = 0.2)

(Bo = 0.2)

(Bo = 0.6)

(Bo = 0.6)

(Bo = 1)

(Bo = 1)

(Bo = 5)

(Bo = 5)

(Bo = 50)

(Bo = 50)

(Bo = 200)

(Bo = 200)

(Bo = 400)

(Bo = 400)

Fig. 14. Effect of particle cohesion on pore characteristics in a spread powder layer. Density pores are coloured by their orientation relative to the spreading direction. Chamber pores are coloured by their pore size.

attributed to the increase of interparticle cohesion. However, when $Bo > 200$, It becomes very difficult for the particles to escape from the blade gap due to the formation of a static assembly in front of the blade and consequently less particles are deposited on the layer and particle distribution becomes sparser.

In summary, the increase of particle cohesion leads to four competing mechanisms affecting the structure of a spread powder layer: 1) an inhomogeneous distribution for non-cohesive and weakly cohesive powders (i.e. $Bo \leq 1$) due to collision-induced particle clustering, 2) an

enhanced layer homogeneity for moderately cohesive powders (i.e. $1 < Bo \leq 50$) due to the increase of particle-wall adhesion, 3) a reduction in layer homogeneity when further increasing interparticle cohesion (i.e. $50 < Bo \leq 200$) due to the formation of chain-like clusters by strong interparticle attractive forces, and 4) particles being stripped off the base of a static assembly for strongly cohesive powders (i.e. $Bo > 200$).

It is worthwhile to mention that particle sliding will certainly be hindered if spreading over a rough surface formed by pre-melted/
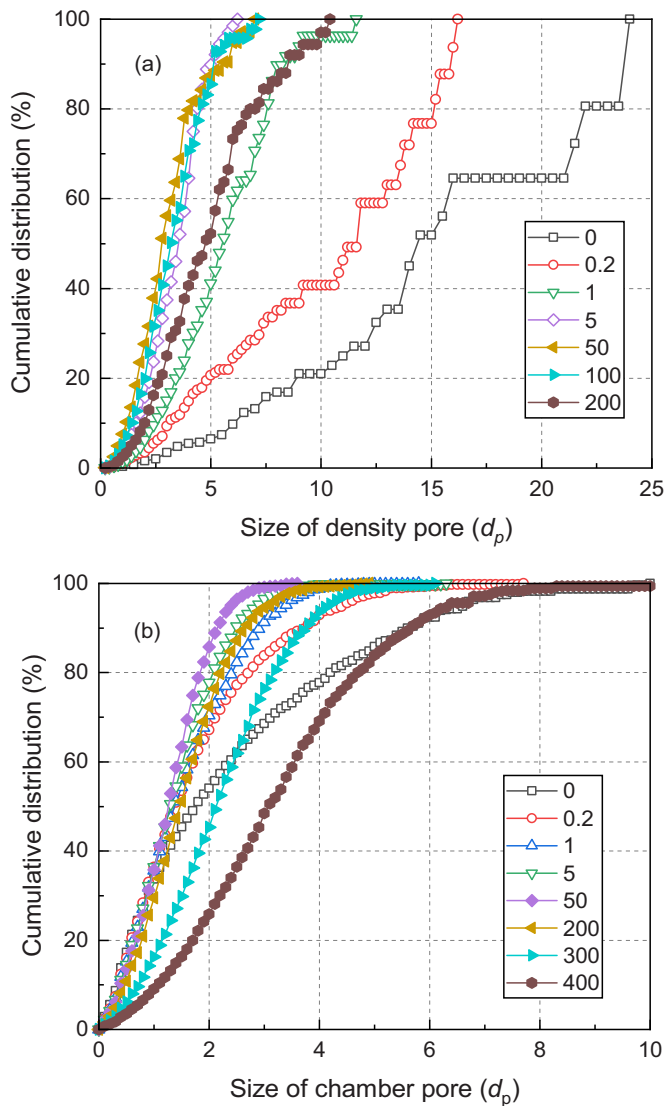
Fig. 15. Effect of particle cohesion on the cumulative size distribution of (a) density pore and (b) chamber pore.

Fig. 16. Effect of particle cohesion on the probability density distribution of the size of chamber pore.

sintered powder. Interlocking with the substrate may also occur, but the extent of which depends on surface morphology, particle size, shape, cohesiveness, and subjected stress. For SLM, the surface roughness can be in the order of 10 μm, spreading of small particles are thus expected to be affected more than that of larger particles. Moreover, weakly cohesive particles can be more affected than that of strongly cohesive particles, due to a larger particle mobility after being discharged from the blade gap. As the analysis performed in this paper is based on a small blade clearance, further study on the interaction between particle cohesion and blade clearance are worthwhile. Increasing the blade clearance allows more particles to be discharged, therefore, the empty patches observed in the present study may vanish. For weakly cohesive particles, particle rearrangement can be enhanced so that layer homogeneity and mean packing density can be improved. However, a more realistic contact force model should not have a significant influence on the results presented here, as cohesion force plays a dominant role in determining the sliding and rolling resistances for cohesive fine particles.

6. Conclusions

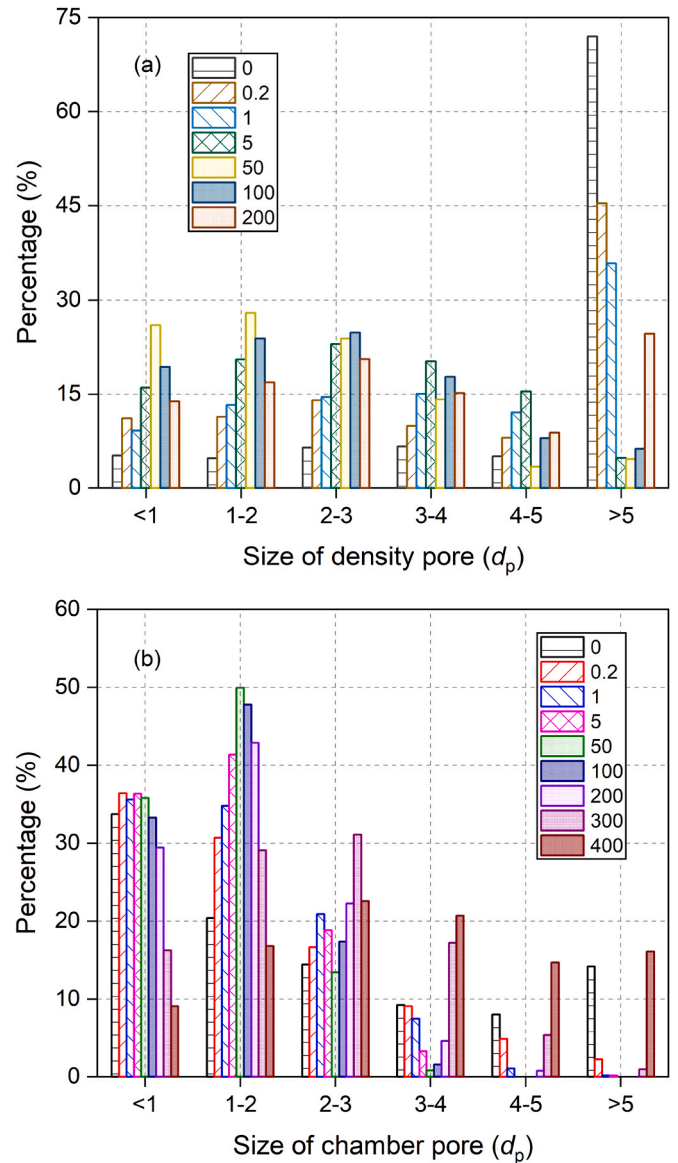In the present study, a discrete element modelling framework was

established, which combines a stiffness scaling methodology with GPU computing to enable fast and reliable particle-scale simulations of the spreading of cohesive fine powders in powder-bed-based additive manufacturing. Together with a digital-based approach for the characterisation of spread powder layer, a direct link between microscopic particle properties and layer characteristics was established. The role of particle cohesion in the spreading of spherical particles was systematically addressed, where the strength of particle cohesion is quantified by a dimensionless Bond number. The main findings are summarized as follows,

- Particle stiffness can be safely reduced three orders of magnitude for both packing and spreading of cohesive fine powders, confirming the validity of the present approach in handling reduced particle stiffness.
- Particle cohesion has a strong impact on the local structure of a spread powder layer. It prohibits the formation of large agglomerates for weakly cohesive powders while promotes the formation of chain-like structures for strongly cohesive powders. Increasing particle cohesion first decreases and then increases the cluster size, and

making these clusters aligned increasingly perpendicular to the spreading direction.

- The median of local packing density remains relatively stable over a large range of *Bo*, which decreases slightly with particle cohesion up to *Bo* = 200 beyond which a sharp drop is observed.
- The layer characteristics shows a consistent and complex dependence on particle cohesion, as captured by several metrics in terms of local packing density, surface roughness and pore size. For the cases considered here, an optimal level of particle cohesion is found around *Bo* = 50, showing the smallest variations of local packing density, surface roughness and pore sizes.
- Four competing mechanisms are identified regarding the role of particle cohesion on powder spreading, which can be partly interpreted by a dimensionless inertial length.

Although this study presents an idealized spreading of cohesive fine powders, it reveals a more complex spreading behaviour than that might be anticipated. The modelling framework developed in this work represents a critical step towards understanding powder spreading in more realistic systems. Future work includes i) extension to more realistic boundary conditions, including the morphology of substrate and operating temperature, ii) quantitative model validation on the quality of spread powder layer and iii) the influence of material properties and their interaction with process conditions.

CRediT authorship contribution statement

Yi He: Conceptualization, Methodology, Software, Investigation, Validation, Formal analysis, Visualization, Writing - original draft, Writing - review & editing. **Ali Hassanpour:** Writing - review & editing. **Andrew E. Bayly:** Writing - review & editing, Project administration, Funding acquisition.

Declaration of Competing Interest

The authors declare that they have no known competing financial interests or personal relationships that could have appeared to influence the work reported in this paper.

Acknowledgments

Appendix A. Supporting information

Supplementary data associated with this article can be found in the online version at doi:10.1016/j.addma.2020.101685.

References

[1] W.E. Frazier, Metal additive manufacturing: a review, J. Mater. Eng. Perform. 23 (2014) 1917–1928, https://doi.org/10.1007/s11665-014-0958-z.

[2] C.L.A. Leung, S. Marussi, M. Towrie, R.C. Atwood, P.J. Withers, P.D. Lee, The effect of powder oxidation on defect formation in laser additive manufacturing, Acta Mater. 166 (2019) 294–305, https://doi.org/10.1016/j.actamat.2018.12.027.

[3] D. Sofia, D. Barletta, M. Poletto, Laser sintering process of ceramic powders: the effect of particle size on the mechanical properties of sintered layers, Addit. Manuf. 23 (2018) 215–224, https://doi.org/10.1016/j.addma.2018.08.012.

[4] D. Sofia, R. Chirone, P. Lettieri, D. Barletta, M. Poletto, Selective laser sintering of ceramic powders with bimodal particle size distribution, Chem. Eng. Res. Des. 136 (2018) 536–547, https://doi.org/10.1016/j.cherd.2018.06.008.

[5] S. Haeri, S. Haeri, J. Hanson, S. Lotfian, Analysis of radiation pressure and aerodynamic forces acting on powder grains in powder-based additive

manufacturing, Powder Technol. 368 (2020) 125–129, https://doi.org/10.1016/j.powtec.2020.04.031.

[6] S. Haeri, L. Benedetti, O. Ghita, Effects of particle elongation on the binary coalescence dynamics of powder grains for Laser Sintering applications, Powder Technol. 363 (2020) 245–255, https://doi.org/10.1016/j.powtec.2019.12.025.

[7] A. Townsend, N. Senin, L. Blunt, R.K. Leach, J.S. Taylor, Surface texture metrology for metal additive manufacturing: a review, Precis. Eng. 46 (2016) 34–47, https://doi.org/10.1016/j.precisioneng.2016.06.001.

[8] X. Wang, X. Gong, K. Chou, Review on powder-bed laser additive manufacturing of Inconel 718 parts, Proc. Inst. Mech. Eng. Part B J. Eng. Manuf. 231 (2017) 1890–1903, https://doi.org/10.1177/0954405415619883.

[9] C. Körner, E. Attar, P. Heinl, Mesoscopic simulation of selective beam melting processes, J. Mater. Process. Technol. 211 (2011) 978–987, https://doi.org/10.1016/j.jmatprotec.2010.12.016.

[10] Y. Bai , G. Wagner , C.B. Williams , Effect of bimodal powder mixture on powder packing density and sintered density in binder jetting of metals. Proceedings of 26th Annual International solid free Fabry Symptoms Additive manufacturing Conference SFF 2015, 2020 758 771.

[11] Y. Khalil, N. Hopkinson, A. Kowalski, J.P.A. Fairclough, Characterisation of UHMWPE polymer powder for laser sintering, Mater. Basel 12 (2019) 3496, https://doi.org/10.3390/ma12213496.

[12] S.E. Brika, M. Letenneur, C.A. Dion, V. Brailovski, Influence of particle morphology and size distribution on the powder flowability and laser powder bed fusion manufacturability of Ti-6Al-4V alloy, Addit. Manuf. 31 (2020), 100929, https://doi.org/10.1016/j.addma.2019.100929.

[13] C.A. Chatham, T.E. Long, C.B. Williams, A review of the process physics and material screening methods for polymer powder bed fusion additive manufacturing, Prog. Polym. Sci. 93 (2019) 68–95, https://doi.org/10.1016/j.progpolymsci.2019.03.003.

[14] D. Ruggi, M. Lupo, D. Sofia, C. Barrès, D. Barletta, M. Poletto, Flow properties of polymeric powders for selective laser sintering, Powder Technol. 370 (2020) 288–297, https://doi.org/10.1016/j.powtec.2020.05.069.

[15] D. Ruggi, C. Barrès, J.Y. Charmeau, R. Fulchiron, D. Barletta, M. Poletto, A quantitative approach to assess high temperature flow properties of a PA 12 powder for laser sintering, Addit. Manuf. 33 (2020), 101143, https://doi.org/10.1016/j.addma.2020.101143.

[16] S. Vock, B. Klöden, A. Kirchner, T. Weißgärber, B. Kieback, Powders for powder bed fusion: a review, Prog. Addit. Manuf. 4 (2019) 383–397, https://doi.org/10.1007/s40964-019-00078-6.

[17] M. Van den Eynde, L. Verbelen, P. Van, Puyvelde, assessing polymer powder flow for the application of laser sintering, Powder Technol. 286 (2015) 151–155, https://doi.org/10.1016/j.powtec.2015.08.004.

[18] Y.Y. Sun, S. Gulizia, C.H. Oh, C. Doblin, Y.F. Yang, M. Qian, Manipulation and characterization of a novel titanium powder precursor for additive manufacturing applications, JOM 67 (2015) 564–572, https://doi.org/10.1007/s11837-015-1301-3.

[19] M. Ahmed, M. Pasha, W. Nan, M. Ghadiri, A simple method for assessing powder spreadability for additive manufacturing, Powder Technol. 367 (2020) 671–679, https://doi.org/10.1016/j.powtec.2020.04.033.

[20] L. Cordova, T. Bor, M. de Smit, M. Campos, T. Tinga, Measuring the spreadability of pre-treated and moisturized powders for laser powder bed fusion, Addit. Manuf. 32 (2020), 101082, https://doi.org/10.1016/j.addma.2020.101082.

[21] H. Chen, Q. Wei, S. Wen, Z. Li, Y. Shi, Flow behavior of powder particles in layering process of selective laser melting: Numerical modeling and experimental verification based on discrete element method, Int. J. Mach. Tools Manuf. 123 (2017) 146–159, https://doi.org/10.1016/j.ijmachtools.2017.08.004.

[22] L.I. Escano, N.D. Parab, L. Xiong, Q. Guo, C. Zhao, K. Fezzaa, W. Everhart, T. Sun, L. Chen, Revealing particle-scale powder spreading dynamics in powder-bed-based additive manufacturing process by high-speed x-ray imaging, Sci. Rep. 8 (2018) 1–11, https://doi.org/10.1038/s41598-018-33376-0.

[23] L.I. Escano, N.D. Parab, L. Xiong, Q. Guo, C. Zhao, T. Sun, L. Chen, Investigating powder spreading dynamics in additive manufacturing processes by in-situ high-speed X-ray imaging, Synchrotron Radiat. N. 32 (2019) 9–13, https://doi.org/10.1080/08940886.2019.1582281.

[24] C. Meier, R. Weissbach, J. Weinberg, W.A. Wall, A.J. Hart, Critical influences of particle size and adhesion on the powder layer uniformity in metal additive manufacturing, J. Mater. Process. Technol. 266 (2019) 484–501, https://doi.org/10.1016/j.jmatprotec.2019.08.037.

[25] L. Wang, E.L. Li, H. Shen, R.P. Zou, A.B. Yu, Z.Y. Zhou, Adhesion effects on spreading of metal powders in selective laser melting, Powder Technol. 363 (2020) 602–610, https://doi.org/10.1016/j.powtec.2019.12.048.

[26] S. Haeri, Y. Wang, O. Ghita, J. Sun, Discrete element simulation and experimental study of powder spreading process in additive manufacturing, Powder Technol. 306 (2017) 45–54, https://doi.org/10.1016/j.powtec.2016.11.002.

[27] D. Schiochet Nasato, T. Pöschel, Influence of particle shape in additive manufacturing: Discrete element simulations of polyamide 11 and polyamide 12, Addit. Manuf. 36 (2020), 101421, https://doi.org/10.1016/j.addma.2020.101421.

[28] E.J.R.R. Parteli, T. Pöschel, Particle-based simulation of powder application in additive manufacturing, Powder Technol. 288 (2016) 96–102, https://doi.org/10.1016/j.powtec.2015.10.035.

[29] W. Nan, M. Pasha, M. Ghadiri, Numerical simulation of particle flow and segregation during roller spreading process in additive manufacturing, Powder Technol. 364 (2020) 811–821, https://doi.org/10.1016/j.powtec.2019.12.023.

[30] H. Chen, Y. Chen, Y. Liu, Q. Wei, Y. Shi, W. Yan, Packing quality of powder layer during counter-rolling-type powder spreading process in additive manufacturing,

Int. J. Mach. Tools Manuf. 153 (2020), 103553, https://doi.org/10.1016/j.ijmachtools.2020.103553.

[31] W. Nan, M. Pasha, T. Bonakdar, A. Lopez, U. Zafar, S. Nadimi, M. Ghadiri, Jamming during particle spreading in additive manufacturing, Powder Technol. 338 (2018) 253–262, https://doi.org/10.1016/j.powtec.2018.07.030.

[32] S. Haeri, Optimisation of blade type spreaders for powder bed preparation in additive manufacturing using DEM simulations, Powder Technol. 321 (2017) 94–104, https://doi.org/10.1016/j.powtec.2017.08.011.

[33] J. Zhang, Y. Tan, T. Bao, Y. Xu, X. Xiao, S. Jiang, Discrete element simulation of the effect of roller-spreading parameters on powder-bed density in additive manufacturing, Mater. Basel (2020) 2285.

[34] Y.M. Fouda, A.E. Bayly, A DEM study of powder spreading in additive layer manufacturing, Granul. Matter 22 (2020) 1–18, https://doi.org/10.1007/s10035-019-0971-x.

[35] J. Hærvig, U. Kleinhans, C. Wieland, H. Spliethoff, A.L. Jensen, K. Sørensen, T. J. Condra, On the adhesive JKR contact and rolling models for reduced particle stiffness discrete element simulations, Powder Technol. 319 (2017) 472–482, https://doi.org/10.1016/j.powtec.2017.07.006.

[36] K. Washino, E.L. Chan, T. Tanaka, DEM with attraction forces using reduced particle stiffness, Powder Technol. 325 (2018) 202–208, https://doi.org/10.1016/j.powtec.2017.11.024.

[37] Y. He, A. Hassanpour, M.A. Behjani, A.E. Bayly, A novel stiffness scaling methodology for discrete element modelling of cohesive fine powders, Appl. Math. Model. 90 (2021) 817–844, https://doi.org/10.1016/j.apm.2020.08.062.

[38] Y. He, T.J.J. Evans, A.B.B. Yu, R.Y.Y. Yang, A GPU-based DEM for modelling large scale powder compaction with wide size distributions, Powder Technol. 333 (2018) 219–228, https://doi.org/10.1016/j.powtec.2018.04.034.

[39] Y. He, A.E. Bayly, A. Hassanpour, F. Muller, K. Wu, D. Yang, A GPU-based coupled SPH-DEM method for particle-fluid flow with free surfaces, Powder Technol. 338 (2018) 548–562, https://doi.org/10.1016/j.powtec.2018.07.043.

[40] Y. He, F. Muller, A. Hassanpour, A.E. Bayly, A CPU-GPU cross-platform coupled CFD-DEM approach for complex particle-fluid flows, Chem. Eng. Sci. 223 (2020), 115712, https://doi.org/10.1016/j.ces.2020.115712.

[41] Y. He, J. Gardy, A. Hassanpour, A.E. Bayly, A digital-based approach for characterising spread powder bed in additive manufacturing, Mater. Des. 196 (2020), 109102, https://doi.org/10.1016/j.matdes.2020.109102.

[42] Y. He, T.J.J. Evans, Y.S.S. Shen, A.B.B. Yu, R.Y.Y. Yang, Discrete modelling of the compaction of non-spherical particles using a multi-sphere approach, Miner. Eng. 117 (2018) 108–116, https://doi.org/10.1016/j.mineng.2017.12.013.

[43] R.D. Mindlin, H. Deresiewicz, Elastic spheres in contact under varying oblique forces, ASME J. Appl. Mech. (1953) 327–344.

[44] H.C. Hamaker, The London-van der Waals attraction between spherical particles, Physica 4 (1937) 1058–1072, https://doi.org/10.1016/S0031-8914(37)80203-7.

[45] Y. Gu, A. Ozel, S. Sundaresan, A modified cohesion model for CFD-DEM simulations of fluidization, Powder Technol. 296 (2016) 17–28, https://doi.org/10.1016/j.powtec.2015.09.037.

[46] P. Sun, Z.Z. Fang, Y. Xia, Y. Zhang, C. Zhou, A novel method for production of spherical Ti-6Al-4V powder for additive manufacturing, Powder Technol. 301 (2016) 331–335, https://doi.org/10.1016/j.powtec.2016.06.022.

[47] M. Pasha, S. Dogbe, C. Hare, A. Hassanpour, M. Ghadiri, A linear model of elasto-plastic and adhesive contact deformation, Granul. Matter 16 (2014) 151–162, https://doi.org/10.1007/s10035-013-0476-y.

[48] C.L. Martin, L.C.R. Schneider, L. Olmos, D. Bouvard, Discrete element modeling of metallic powder sintering, Scr. Mater. 55 (2006) 425–428, https://doi.org/10.1016/j.scriptamat.2006.05.017.

[49] E.J.R. Parteli, J. Schmidt, C. Blümel, K.E. Wirth, W. Peukert, T. Pöschel, Attractive particle interaction forces and packing density of fine glass powders, Sci. Rep. 4 (2014) 6227, https://doi.org/10.1038/srep06227.

[50] R.Y. Yang, R.P. Zou, A.B. Yu, Computer simulation of the packing of fine particles, Phys. Rev. E 62 (2000) 3900–3908, https://doi.org/10.1103/PhysRevE.62.3900.

[51] K.J. Dong, R.Y. Yang, R.P. Zou, A.B. Yu, Role of interparticle forces in the formation of random loose packing, Phys. Rev. Lett. 96 (2006) 1–4, https://doi.org/10.1103/PhysRevLett.96.145505.

[52] W.D. Fullmer, C.M. Hrenya, The clustering instability in rapid granular and gas-solid flows, Annu. Rev. Fluid Mech. 49 (2017) 485–510, https://doi.org/10.1146/annurev-fluid-010816-060028.